# Design of a High-Speed Ferrite-based Brushless DC Machine for Electric Vehicles

Alfonso Damiano*, Andrea Floris, Giuseppe Fois**,
Ignazio Marongiu*, Mario Porru*, Alessandro Serpi*
*Member, IEEE, **Student Member, IEEE
University of Cagliari, Department of Electrical and Electronic Engineering
Via Marengo 2
09123 Cagliari, Italy
(alfio, andrea.floris, giuseppe.fois, marongiu, mario.porru, alessandro.serpi)@diee.unica.it.

***Abstract* -- In the present paper an analytic procedure for the preliminary design of a High-Speed ferrite-based Brushless DC Machine (HS-BLDC) has been proposed. In particular, a mechanical and electromagnetic modeling has been developed in order to take into account their mutual influence in the definition of the geometry of the electrical machine. In addition, suitable design targets have been imposed in accordance with electric vehicle application requirements. Hence, several mechanical and electromagnetic constraints have been introduced in order to comply with high-speed operation, preventing demagnetization issues of ferrite magnets as well. Subsequently, an HS-BLDC characterized by an inner rotor configuration has been designed in accordance with the proposed methodology. The analytical procedure and the corresponding results have been reported and validated by means of Finite Element Analyses (FEAs), highlighting the effectiveness of the proposed configuration and design solutions.**

***Index Terms*—Design methodology, Ferrites, Finite element methods, High-speed machines, Permanent magnet machines**

## I. Introduction

High-Speed Electrical Machines (HSEMs) are characterized by rated speed from 10 krpm to over 200 krpm and rated power from few watts to hundreds of kilowatts. They have been used for a long time due to their numerous advantages, among which high power density and efficiency, reduced size, weights and overall costs. Hence, HSEMs are currently employed in a wide range of applications, such as dental drills and medical surgery tools, flywheel energy storage systems, gas and oil compressors, spindles and power generation [1]–[3]. Several kinds of electrical machines can be considered for HSEMs depending on the specific application, e.g. induction machines, permanent magnet synchronous machines and switched reluctance machines. Particularly, novel materials and recent improvements in power electronics and control systems are enabling a further increase of HSEM performances and speed operating range [4], making them suitable also for electric propulsion systems. In this regard, one of the main challenges is related to the need of high gear ratios in order to guarantee an appropriate coupling between HSEM and wheels. Particularly, the use of a single mechanical gear characterized by a high gear ratio seems not a suitable solution because it increases volume and weight of the propulsion system significantly, reducing its overall efficiency as well. Alternatively, multiple mechanical gears with relatively low gear ratios may be employed, which are series-connected in order to enable a sequential reduction of HSEM speed. This configuration limits volume and weight increase compared to the previous solution, as pointed out in [5], but still suffers from efficiency issues due to high mechanical losses. A very promising solution consists of magnetic gears, which are characterized by high gear ratios, reduced volume and weight, as well as by high efficiency. As a result, the use of HSEM combined with a suitable transmission system (series-connected and/or magnetic) allows a 20% reduction of volume and weight of Electric Vehicle (EV) propulsion system compared to those actually available on the market [5].

Among the several kinds of HSEM, High-Speed Permanent Magnet Synchronous Machines (HS-PMSMs) are very popular, especially for low-power applications [6], [7]. One of the main challenge in designing an HS-PMSM is surely the significant mechanical forces acting on the rotor due to the high speed, which have to be taken into account properly. Hence, Permanent Magnets (PMs) are usually glued to the rotor yoke and contained by mechanical sleeves. The latter are made up of high-strength materials, such as metallic alloys or carbon fibers [8]. Furthermore, rare-earth PMs are typically used due to their high-energy density, which limits rotor size and, thus, peripheral speed. However, there is a great concern about using rare-earth PMs due to availability and price fluctuation issues. Consequently, the use of less rare-earth or no rare-earth PMs is considered a viable solution, especially in a growing sector as automotive [9]. Particularly, the employment of ferrite PMs does not imply reduced HS-PMSM performances, it enabling significant cost saving [10], [11]. However, ferrite-based HS-PMSMs still suffer from relatively low torque and power density, as well as from some critical issues related to weak residual magnetism and low coercive force.

In this context, the preliminary design of a novel High-Speed ferrite-based Brushless DC machine (HS-BLDC) suitable as the propulsion motor of light-duty EVs is presented in this paper [12]. Particularly, based on the design targets (40 kW, 12.7 Nm, 30-100 krpm), an HS-PMSM has been identified as the most suitable HSEM configuration, especially in terms of efficiency. In addition, since high torque density is not mandatory due to the high-speed operating range (30-100 krpm), no rare-earth PMs have been selected with the aim of limiting electrical machine costs

© 2017 IEEE. Personal use of this material is permitted. Permission from IEEE must be obtained for all other uses, in any current or future media, including reprinting/republishing this material for advertising or promotional purposes, creating new collective works, for resale or redistribution to servers or lists, or reuse of any copyrighted component of this work in other works. Published paper's DOI: 10.1109/TIA.2017.2699164

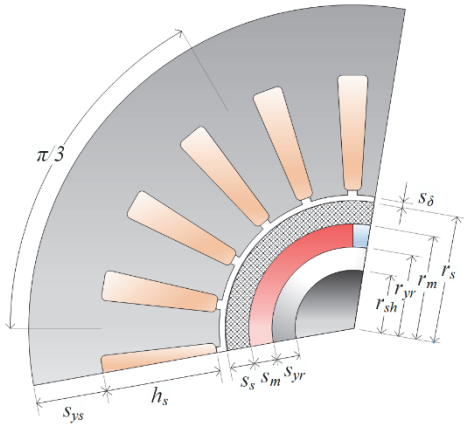


Fig. 1. Cross section of the proposed machine geometry.

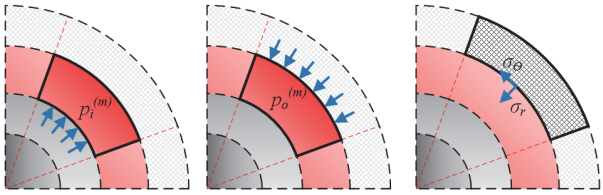


Fig. 2. Cross section of the rotor: shaft (dark gray) and yoke (light gray), PMs (red) and sleeve (dotted black).

and PM availability issues. A Brushless DC configuration has been thus chosen with the aim of achieving higher torque density and/or lower Joule losses compared to Brushless AC solutions [13]. In addition, a sleeved surface-mounted PM configuration has been chosen, since it enables high peripheral speeds [14]. Hence, mechanical and electromagnetic modeling has been considered, based on which the analytical design of the HS-BLDC has been carried out. This is done in accordance with both design targets and operating constraints; the former have been set in accordance with EV application requirements, whereas operating constraints are related mainly to high-speed operation and PM demagnetization issues. The proposed design approach has been validated through extensive simulation studies, which have been performed by means of Finite Element Analyses (FEAs) that regard both mechanical and electromagnetic aspects.

## II. HS-PMSM Modeling

The mechanical modeling of the HS-PMSM rotor is fundamental because the mechanical stress related to high rotational speed is not negligible, requiring the definition of appropriate mechanical constraints. These affect the HS-PMSM rotor geometry, especially the PM configuration. In fact, PM materials generally present better mechanical properties to compression stress rather than to tensile stress. Therefore, for an inner rotor HS-PMSM configuration, the PMs are enclosed by a mechanical sleeve in order to limit tensile stress and guarantee their retention, especially at high-speed operation.

Electromagnetic modeling is also very important for HS-PMSMs, especially when ferrite PMs are employed. Particularly, due to low residual magnetic flux density and coercive force, PM demagnetization has to be avoided over any operating conditions. For this purpose, the magnetic flux path has to be considered carefully, as well as the effects of the stator current.

Hence, based on the previous considerations, both mechanical and electromagnetic models are presented in the following subsections.

### A. Mechanical Model

The mechanical model has been developed referring to the machine structure shown in Fig. 1. Particularly, the rotor is made up of an inner shaft, a rotor yoke, a layer of ferrite PMs and an outer sleeve, as highlighted in Fig. 2. In addition, in order to increase mechanical retention, the sleeve is prestressed, i.e. the inner radius of the sleeve surrounding the PMs is smaller than the free outer radius of PMs due to mechanical pretension.

In order to develop the mechanical model, the inner sleeve surface, which is the most critical one, has been considered as the reference geometric structure. Due to the cylindrical symmetry and assuming a relative short axial length, the stress tensor acting on the rotor structure consists of just radial and tangential components ($\sigma_r$ and $\sigma_\theta$ respectively) because axial component ($\sigma_z$) can be considered negligible. Hence, the overall stress on the inner surface of the sleeve can be expressed as the Von Mises equivalent stress:

$$\sigma_{eq} = \sqrt{\sigma_r^{\,2} + \sigma_\theta^{\,2} - \sigma_r \sigma_\theta} \tag{1}$$

where $\sigma_r$ and $\sigma_\theta$ are the radial and tangential stresses. Both $\sigma_r$ and $\sigma_\theta$ consist of two contributions mainly: one is due to the prestress procedure, whereas the other one is caused by rotational motion. Assuming the material linear and isotropic from a mechanical point of view, $\sigma_r$ and $\sigma_\theta$ are expressed as

$$\sigma_x = \sigma_{x,p} + \sigma_{x,\omega} \quad , \quad x \in \{r, \theta\} \tag{2}$$

in which $\sigma_{x,p}$ and $\sigma_{x,\omega}$ are the prestress and the speed component respectively. Consequently, radial components of mechanical stress can be calculated as

$$\sigma_{r,p} = -p_o^{(m)} \tag{3}$$

$$\sigma_{r,\omega} = 0 \tag{4}$$

where $p_o^{(m)}$ is the pressure exerted by sleeve on the outer PMs' surface, as highlighted in Fig. 2. This can be expressed as

$$p_o^{(m)} = \frac{C_{\omega 2} K_2 - C_{\omega 1} K_4 + D K_4}{K_1 K_4 - K_3 K_2} \tag{5}$$

in which $D$ is the radial interference, while $K_1$, $K_2$, $K_3$, $K_4$, $C_{\omega 1}$ and $C_{\omega 2}$ depend on machine parameters, material properties and rotational speed [15], as detailed in the Appendix. Whereas

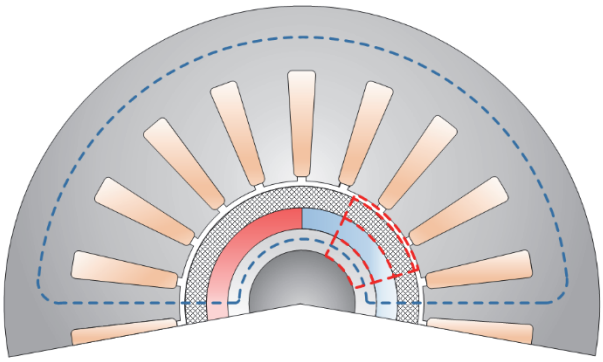

Fig. 3. Closed magnetic flux path (blue) and surfaces (red) considered for Ampère's and Gauss' Laws implementation.

the tangential stress components are expressed as

$$\sigma_{\theta,p} = p_o^{(m)} \frac{\left(r_{yr}+s_m+s_s\right)^2+\left(r_{yr}+s_m\right)^2}{\left(r_{yr}+s_m+s_s\right)^2-\left(r_{yr}+s_m\right)^2} \tag{6}$$

$$\sigma_{\theta,\omega} = \frac{\left(3+\upsilon_s\right)\left(r_{yr}+s_m+s_s\right)^2+\left(1-\upsilon_s\right)\left(r_{yr}+s_m\right)^2}{4}\rho_s\omega_m^2 \tag{7}$$

in which $\omega_m$ is the mechanical speed, $r_{yr}$ is the inner PM radius and $s_m$ and $s_s$ are the PM and sleeve thicknesses respectively. In addition, $\upsilon_s$ and $\rho_s$ are the Poisson ratio and the specific mass density of the sleeve material.

Focusing now on the inner PM surface, the pressure exerted by PMs on the rotor yoke is

$$p_i^{(m)} = \frac{C_{\omega 1}K_3 - C_{\omega 2}K_1 - DK_3}{K_1K_4 - K_3K_2}. \tag{8}$$

It is worth noting that $p_i^{(m)}$ decreases as the speed increases. Hence, the sleeve must be prestressed appropriately in order to ensure the adhesion between PMs and the rotor yoke at the designed maximum speed, thus compensating for centrifugal force.

Mechanical modeling has to account also for the issues related to critical speed in order to avoid resonance phenomena. Particularly, HSEMs cannot operate at speed values too close to the critical one. A generic rotating shaft is characterized by several critical speeds [2], but only the first (minimum) critical speed ($\omega_{m,cr}$) is usually considered in the design process. This is the case of the proposed HS-BLDC, for which the speed constraint can be expressed as

$$\omega_{m,\max} < \omega_{m,cr} \tag{9}$$

Among the different analytic formulations of critical speed reported in the technical literature, the following equation has been here adopted:

$$\omega_{m,cr} = \sqrt{\frac{12\cdot\pi\cdot E_{sh}\cdot r_{sh}^4}{M\cdot l_{sh}^3}} \tag{10}$$

in which $M$ is the total rotor mass, $r_{sh}$ and $l_{sh}$ are shaft radius and bearings distance respectively, $E_{sh}$ being the Young's modulus of the shaft material.

### B. Electromagnetic Model

The HS-PMSM electromagnetic model has been developed by applying both the Ampère's Law and the Gauss' Law to the main magnetic flux path of the machine. These highlight the dependence of the electromagnetic properties on the main machine geometry parameters, among which PM and sleeve thickness.

Therefore, considering the application of the Ampère's Law to the closed magnetic flux path depicted in blue in Fig. 3, the following equation can be deduced:

$$2\int_0^{s_m}\left(\frac{B_m}{\mu_m}+H_c\right)ds + 2\int_0^{s_b}\frac{B_s}{\mu_0}ds + 2\int_0^{s_\delta}\frac{B_\delta}{\mu_0}ds = n\cdot I_{eq} \tag{11}$$

where $H_c$ is the PM coercive force, $B_m$, $B_s$ and $B_\delta$ are the magnetic flux densities within PMs, sleeve and air gap respectively, whereas $\mu_m$ is the PM magnetic permeability. Moreover, $I_{eq}$ and $n$ are the equivalent current and the number of turns of a generic phase winding, whose product is thus the overall magnetomotive force (mmf). Referring to (11), it is worth noting that the iron contributions to the overall magnetic flux path have been neglected. This assumption is quite reasonable due to the large equivalent air gap, which has to account for sleeve thickness. Furthermore, low magnetic flux density is foreseen due to the employment of ferrite-based PMs, thus magnetic saturation effects should not occur. Still referring to (11), it is also worth underlining that only the radial component of the magnetic flux density is considered within PMs, sleeve and the air gap.

Subsequently, the Gauss' Law is applied to the closed surfaces red-highlighted in Fig. 3, which envelope the separation surfaces between:

- rotor yoke and PMs;
- PMs and sleeve;
- sleeve and air gap.

Hence, still assuming the magnetic flux density characterized by the radial component only, (12), (13) and (14) can be achieved:

$$B_m(s) = B_m^{(0)}\frac{r_{yr}}{r_{yr}+s}\quad,\quad s\in\left[0,s_m\right] \tag{12}$$

$$B_s(s) = B_m^{(0)}\frac{r_{yr}}{r_{yr}+s_m+s}\quad,\quad s\in\left[0,s_s\right] \tag{13}$$

$$B_\delta(s) = B_m^{(0)}\frac{r_{yr}}{r_{yr}+s_m+s_b+s}\quad,\quad s\in\left[0,s_\delta\right] \tag{14}$$

where $B_m^{(0)}$ is the magnetic flux density on the contact surface between PMs and the rotor yoke. Therefore, by substituting (12) through (14) in (11), the following result is achieved:

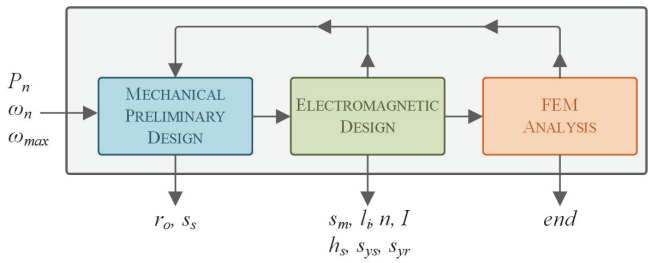


Fig. 4. Workflow of the proposed HS-BLDC design procedure.

$$B_m^{(0)}\left[\frac{r_{yr}}{\mu_m}\ln\left(1+\frac{s_m}{r_{yr}}\right)+\frac{r_{yr}}{\mu_0}\ln\left(1+\frac{s_b+s_\delta}{r_{yr}+s_m}\right)\right]+s_m H_c=\frac{n I_{eq}}{2}. \quad (15)$$

Considering negligible the saturation phenomena, the principle of superimposition can be applied in order to define the design criterion for preventing PM demagnetization due to stator mmf. Particularly, the magnetic flux density due the stator mmf ($\tilde{B}_m$) can be imposed lower than that due to PMs ($\bar{B}_m$) by introducing a coefficient $\alpha$ within (0,1) so that

$$\tilde{B}_m^{(0)}=\alpha\bar{B}_m^{(0)}. \quad (16)$$

Hence, considering no current flowing in the stator windings, (15) becomes

$$\bar{B}_m^{(0)}\left[\frac{r_{yr}}{\mu_m}\ln\left(1+\frac{s_m}{r_{yr}}\right)+\frac{r_{yr}}{\mu_0}\ln\left(1+\frac{s_b+s_\delta}{r_{yr}+s_m}\right)\right]=-s_m H_c. \quad (17)$$

Whereas by imposing $H_c$ equal to zero in (15), the following relationship is achieved:

$$\tilde{B}_m^{(0)}\left[\frac{r_{yr}}{\mu_m}\ln\left(1+\frac{s_m}{r_{yr}}\right)+\frac{r_{yr}}{\mu_0}\ln\left(1+\frac{s_b+s_\delta}{r_{yr}+s_m}\right)\right]=\frac{n I_{eq}}{2}. \quad (18)$$

Consequently, by substituting (17) and (18) in (16), the following expression is obtained

$$n\cdot I_{eq}=-\alpha\cdot 2 s_m H_c. \quad (19)$$

In conclusion, based on (19), it is possible to determine the most suitable magnet thickness in accordance with PM coercive force and required stator mmf, for a given $\alpha$ value.

## III. HS-BLDC Design

The machine design has been carried out referring to a three-phase HS-BLDC and considering the analytical formulation described in the previous section. After defining the design targets of the HS-BLDC, a preliminary mechanical design of the sleeve has been carried out. Subsequently, based on the machine geometry that satisfies the mechanical constraints, the electromagnetic design has been accomplished. The iterative procedure depicted in Fig. 4 has steered towards a final geometry that satisfies all the design targets and both mechanical and electromagnetic constraints.

### A. Design Targets

The HS-BLDC proposed in this paper should be characterized by rated power and speed equal to 40 kW and 30 krpm respectively. Consequently, the rated torque should be equal to about 12.7 Nm. These values have been chosen by considering a light duty EV. In addition, in order to be suitable for automotive applications, a wide constant-power speed range is foreseen. Hence, the maximum speed ($\omega_{m,max}$) is set to 100 krpm as the design target in order to enable HS-BLDC to be coupled with a magnetic gear and a single gear transmission system characterized by a gear ratio of 20 and 4 respectively.

Regarding electromagnetic aspects, the coefficient $\alpha$ has been set to 0.7 in order to prevent PM demagnetization. Particularly, $\alpha = 0.7$ entails that stator current would reduce PM magnetic flux density down to 30% at most at rated operating condition. This would prevent PM demagnetization issues at any speed, ensuring good flux-weakening capability at the same time. Due to high-speed operation, the number of magnetic poles have been set to 2. Regarding winding configuration, a three-phase winding characterized by 3 slots per pole per phase has been considered. In conclusion, the DC-link voltage has been imposed equal to 720 V in accordance with typical values occurring and foreseeing for EVs [16], [17], as well as with HS-BLDC control needs.

### B. Mechanical Design

The mechanical design has been carried out with the aim of maximizing the rotor radius. This has been done with a dual purpose; on one hand, the rotor has to host a large volume of PMs due to their low-energy density. On the other hand, there is the need of reducing the electrical machine axial length ($l_i$) in order to increase the critical speed, which has to be fairly greater than $\omega_{m,max}$. Hence, sleeve thickness ($s_s$) has to be determined together with the outer rotor radius ($r_m$). In order to comply with the design targets, appropriate PM, sleeve and rotor materials have been chosen, whose main properties are reported in Table I. Particularly, a Carbon Fiber Reinforced Polymer (CFRP) has been selected due to its high maximum stress ($\sigma_{s,max}$) and low mass density ($\rho_s$), easing the satisfaction of mechanical constraints. These regard both equivalent stress and contact pressure and must be verified at the maximum speed as

$$\sigma_{eq}\Big|_{\omega=\omega_{m,max}}<\sigma_{sl,max} \quad (20)$$

$$p_i^{(m)}\Big|_{\omega=\omega_{m,max}}>0. \quad (21)$$

Hence, in order to carry out the mechanical design, the evolution of both $\sigma_{eq}$ and $p_o$ as a function of $r_m$ and $s_s$ have been considered, as depicted in Fig. 5. It can be noticed that $\sigma_{eq}$ reaches its minimum value for a given outer rotor radius, whereas it is slightly affected by sleeve thickness. Regarding the contact pressure, it decreases as the outer rotor radius increases, whereas it increases with the sleeve thickness.

TABLE I
MATERIAL PROPERTIES

| Description | Symbol | Unit | Value |
|---|---|---|---|
| ***Sleeve (CFRP 60%)*** | | | |
| Specific mass density | $\rho_s$ | kg/m$^3$ | 1500 |
| Young modulus | $E_s$ | GPa | 240 |
| Poisson ratio | $\upsilon_s$ | [-] | 0.30 |
| Maximum stress | $\sigma_{s,max}$ | GPa | 2.4 |
| ***Rotor and Stator Cores (M235-35A)*** | | | |
| Specific mass density | - | kg/m$^3$ | 7600 |
| Resistivity | - | μΩ·cm | 59 |
| ***Permanent Magnets (Ferrite FB14H TDK)*** | | | |
| Specific mass density | $\rho_m$ | kg/m$^3$ | 5100 |
| Coercive force | $H_c$ | A/m | 330000 |
| Residual magnetism | - | T | 0.435 |

Consequently, outer rotor radius can be maximized in order to reduce overall stress unless this does not imply violating (21). Therefore, rotor radius has been chosen equal to 45 mm and the sleeve thickness has been set to 10 mm, as highlighted in Fig. 5.

## C. Electromagnetic Design

Once a preliminary rotor configuration has been defined, the electromagnetic design can be carried out. Therefore, the expression of the rated power of a Brushless DC machine is considered as

$$P = 2 \cdot E \cdot I \tag{22}$$

where the back-emf magnitude ($E$) and the phase current ($I$) can be further expressed respectively as

$$E = \Lambda \cdot p \cdot \omega_m \quad , \quad I = \frac{I_{eq}}{2} \tag{23}$$

in which $p$ denotes the pole pairs, whereas $\Lambda$ is the magnetic flux linkage due to PMs only. Consequently, considering a three-phase winding in which each phase is distributed uniformly over an angular sector of π/3 per pole, $\Lambda$ can be determined as

$$\Lambda = 2 \cdot n \cdot l_i \cdot r_{yr} \cdot \overline{B}_m^{(0)} \tag{24}$$

in which $r_{yr}$ denotes the inner PM radius. Thus, the substitution of both (23) and (24) in (22) yields

$$P = 2 \cdot p \cdot \omega_m \cdot n \cdot I_{eq} \cdot r_{yr} \cdot l_i \cdot \overline{B}_m^{(0)} \tag{25}$$

The low-energy density and coercive force of PMs require limiting the rated stator current in order to prevent PM demagnetization. This is fundamental for HS-PMSMs with a wide constant-power region, since they resort to high currents at high speeds during flux-weakening operation. Therefore, by combining (25) with both (17) and (19), the following relationship is achieved:

$$\alpha = \frac{\frac{r_{yr}}{\mu_m}\ln\left(1+\frac{s_m}{r_{yr}}\right)+\frac{r_{yr}}{\mu_0}\ln\left(1+\frac{s_b+s_\delta}{r_{yr}+s_m}\right)}{4 \cdot p \cdot \omega_m \cdot l_i \cdot r_{yr} \cdot \left(s_m \cdot H_c\right)^2} P \,. \tag{26}$$

Based on (26), it is possible to determine appropriate loci on the ($s_m$,$l_i$) plane that correspond to different $\alpha$ values, as depicted in Fig. 6. It can be seen that different combinations of $s_m$ and $l_i$ determine the same $\alpha$ value, which has to be 0.7 in accordance with the design target. Hence, among all the available solutions, $s_m$ and $l_i$ have been chosen equal to 10 mm and 155 mm respectively. This choice enables a critical speed of about 194 krpm in accordance with (10) and assuming that $l_{sh}$ is 1.3 times the machine active length ($l_i$).

Once $s_m$ and $l_i$ have been set, $n$ and $I$ values have been determined in order to achieve the design targets. Particularly, $n$ can be calculated by imposing the maximum voltage at rated speed as

$$2E \le \gamma \cdot V_{dc} \tag{27}$$

in which $V_{dc}$ is the DC-link voltage and $\gamma$ is an a-dimensional coefficient, which is imposed less than 1 in order to account for additional voltage drops and HS-BLDC

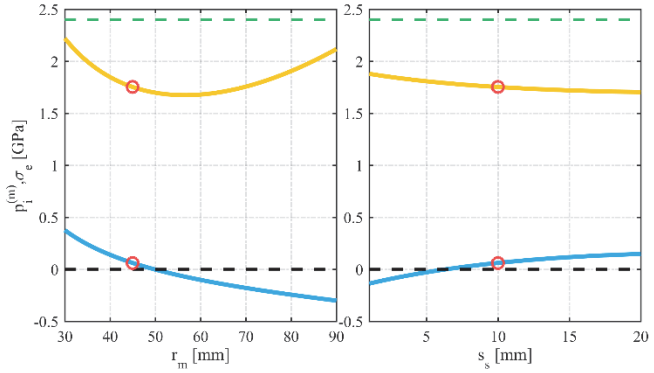


Fig. 5. The evolution of $\sigma_{eq}$ (yellow) and $p_i^{(m)}$ (cyan) with $r_m$ (on the left) and $s_s$ (on the right) at 100 krpm, together with $\sigma_{s,max}$ of the CFPR (green). The red circles highlight the selected configuration.

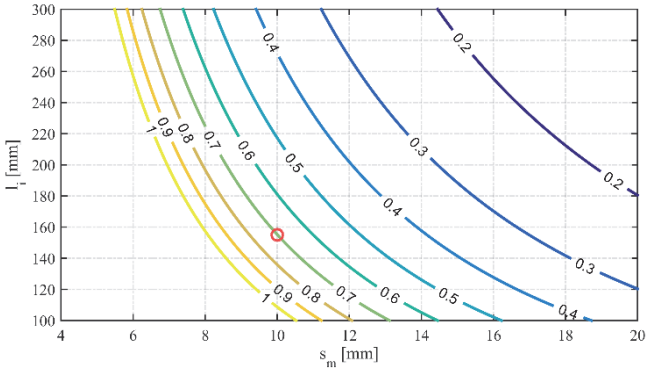


Fig. 6. The constant-α loci on the ($s_m$,$l_i$) plane. The red circle highlights the selected configuration.

controllability at any speed [18]. Hence, by substituting (19), (22) and (23) in (27), the following relationship is achieved:

$$n \le -\frac{\gamma \cdot V_{dc} \cdot \alpha \cdot s_m \cdot H_c}{P}. \quad (28)$$

Assuming negligible voltage drops due to stator resistance, inductive voltage drops due to stator inductance and torque current at rated speed have to be considered. These occur due to the employment of a three-phase-on control approach [19], which guarantees enhanced performances in terms of both reduced torque ripple and Joule losses compared to conventional current commutation controls, as pointed out in [20]. Consequently, assuming inductive voltage drops to be about $\alpha$ times the back-emfs due to PM in accordance with (16) and that they occur on the quadrature axis, $\gamma$ can be chosen in accordance with the following inequality:

$$\gamma \le \frac{1}{\sqrt{1+\alpha^2}}. \quad (29)$$

Hence, based on (29), γ has been set to 0.6 in order to enable a wide Constant Power Speed Range (CPSR), as well as for ensuring high HS-BLDC dynamic performances at any speed [21]. As a result, $n$ has been set to 24 in accordance with (28) . Consequently, based on (19) and (23), a phase current value of about 98 A is achieved.

In conclusion, the main design parameters of the proposed HS-BLDC are summed up in Table II, together with its rated values. Particularly, the last stage of the electromagnetic design has regarded the HS-BLDC stator. Referring to phase windings, it is necessary to choose a wire size which can guarantee the same performances in each operating condition. Then a wire size of 6 mm$^2$ has been chosen. Hence, by imposing a maximum current density of 3 A/mm$^2$, a configuration with 6 parallel wires has been considered for each turn. Subsequently, the slot fill factor and the ratio between slot and tooth widths have been set both to 0.54. Hence, slot sizes have been calculated, whereas stator yoke width has been determined in order to achieve fair values of magnetic flux density, by taking into account also the necessity to minimize iron losses at high-speed operation.

### *D. Weight, volume and cost analysis*

In order to assess the benefits of employing the proposed HS-BLDC within an electric propulsion system of a light duty EV, a detailed analysis of volumes, weights and costs has been carried out, as reported in Table III. It can be seen that the cost of low-energy density PMs is very low compared to the overall HS-BLDC cost (about 3%), as expected. Regarding the inverter, the analysis has been focused on a 50 kVA Silicon Carbide (SiC) inverter; this is due to the need of a high switching frequency (around 100 kHz) in order to drive the HS-BLDC by the three-phase-on control approach previously mentioned. Finally, the cost of the magnetic gear has been estimated based on [22], revealing this as the most expensive element of the overall propulsion system. This is due mainly to the still poor availability of magnetic gears on the market. However, it is worth noting that this technology is experiencing an increasing interest and growth in several sectors, which should lead to cost reductions, even in the short term.

TABLE II
MACHINE PARAMETERS AND RATED VALUES

| Description | Symbol | Unit | Value |
|---|---|---|---|
| Rated power | $P_n$ | kW | 40 |
| Rated speed | $\omega_{m,n}$ | krpm | 30 |
| Maximum speed | $\omega_{m,max}$ | krpm | 100 |
| Rated torque | $T_e$ | Nm | 12.73 |
| Rated current | $I_n$ | A | 98 |
| Pole pairs | $p$ | [-] | 1 |
| Phase resistance | $R$ | mΩ | 22 |
| Phase inductance | $L$ | μH | 667 |
| Magnetic ratio | $\alpha$ | [-] | 0.70 |
| Radial interference | $D$ | mm | 0.3 |
| Shaft radius | $r_{sh}$ | mm | 25 |
| Rotor yoke thickness | $s_{yr}$ | mm | 10 |
| PM thickness | $s_m$ | mm | 10 |
| Sleeve thickness | $s_s$ | mm | 10 |
| Air-gap | $s_\delta$ | mm | 1.5 |
| Stator outer radius | $r_{ys}$ | mm | 140 |
| Stator yoke | $s_{ys}$ | mm | 30.6 |
| Slot height | $h_s$ | mm | 51.4 |
| Active length | $l_i$ | mm | 155 |
| Bearings distance | $l_{sh}$ | mm | 201 |

TABLE III
VOLUMES, WEIGHTS AND COSTS ANALYSIS

| Description | Volume [dm$^3$] | Weight [kg] | Cost [€] |
|---|---|---|---|
| Iron core | 6.89 | 52.12 | 209 |
| Copper | 1.1 | 10.0 | 80 |
| Shaft | 0.43 | 3.51 | 11 |
| PM | 0.39 | 1.99 | 10 |
| Sleeve | 0.48 | 0.73 | 14 |
| **Total (HS-BLDC)** | **9.29** | **68.35** | **324** |
| Inverter | 3.7 | 3.5 | 150 |
| Magnetic gear | 3.5 | 26.5 | 381 |
| **Total** | **16.49** | **98.35** | **855** |

## IV. Finite Element Analyses

In order to verify the proposed HS-BLDC configuration, extensive Finite-Element Analyses (FEAs) have been carried out by means of Solidworks and JMAG. This is done in order to corroborate the effectiveness of the proposed preliminary design, which has been accomplished by means of the analytic procedure described in the previous section.

The FEA simulation regard the mechanical forces on the sleeve and on the PMs at first, i.e. the $\sigma_{eq}$ and $p_i^{(m)}$ space distributions. Particularly, the distribution of $\sigma_{eq}$ at $\omega_{m,max}$ is shown in Fig. 7. It can be seen that $\sigma_{eq}$ is higher on the inner surface of the sleeve, whereas it decreases rapidly along the radial direction, as expected. The maximum equivalent stress value is about 1766 MPa, which is much lower than the maximum stress allowable by the CFRP (2400 MPa). In addition, the corresponding $p_i^{(m)}$ distribution shown in Fig. 8 reveals that $p_i^{(m)}$ is about 68 MPa, thus guaranteeing appropriate adhesion between PMs and rotor yoke at any speed.

The electromagnetic FEA results at rated speed and torque are reported in Fig. 9 and Fig. 10. Particularly, the magnetic flux density distribution shown in Fig. 9 reveals quite low values compared to magnetic saturation thresholds of the iron core material (1.3 T), thus confirming the validity of the assumptions made during the electromagnetic modeling. In this context, it is worth noting that Fig. 9 reveals a poor HS-BLDC magnetic exploitation. However, this is required in order to limit iron losses and back-emfs, especially at high-speed operation. The phase back-emfs evolutions depicted in Fig. 10 highlight good trapezoidal shapes, quite similar to the ideal ones, their magnitudes complying with the voltage constraint imposed by (27). In addition, Fig. 10 shows also the electromagnetic torque evolution at rated speed, which is achieved by supplying the HS-BLDC in accordance with the three-phase-on control approach [20]. Even in this case, simulation results point out the presence of a limited torque ripple (about 5%), revealing the effectiveness of the proposed design. In addition, the chosen control approach enables good HS-BLDC performances in terms of maximum torque at rated speed (1.43 pu) and wide CPSR (from 30 krpm to 100 krpm), as well as no demagnetization issues at any speed, as highlighted in Fig. 11 and Fig. 12. In conclusion, the good matching between analytical and FEA results are highlighted in Table IV, although some differences occur regarding the electromagnetic aspects. Particularly, magnetic flux densities achieved by FEA are lower than expected, leading to reduced torque and power. This can be justified mainly by the fact that the analytical procedure does not account for the iron contributions of the magnetic flux path, thus leading to an overestimation of the magnetic flux density. Consequently, if magnetic saturation occurs (which is not the case of the proposed HS-BLDC), the design procedure needs to be

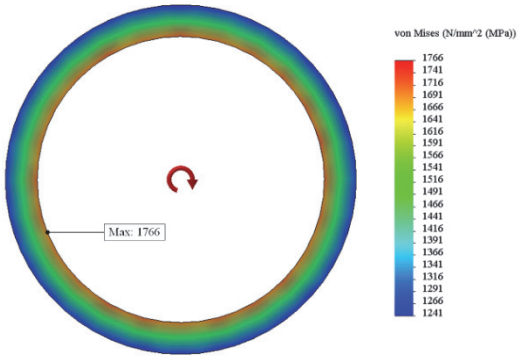


Fig. 7. Equivalent stress on the inner surface of the sleeve at $\omega_{m,max}$.

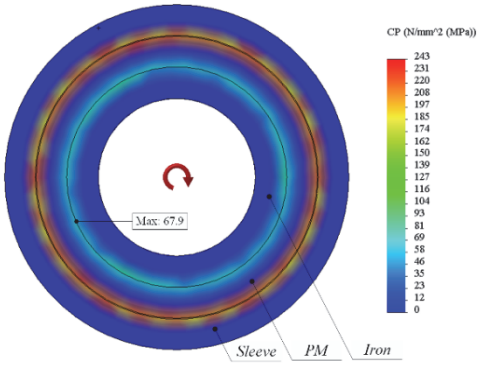


Fig. 8. Contact pressure on the rotor surface at $\omega_{m,max}$.

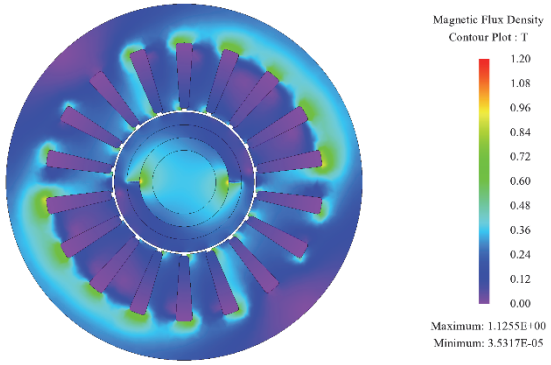


Fig. 9. Magnetic flux density at $\omega_m$ = 30 krpm and $T_e$ = 12.56 Nm.

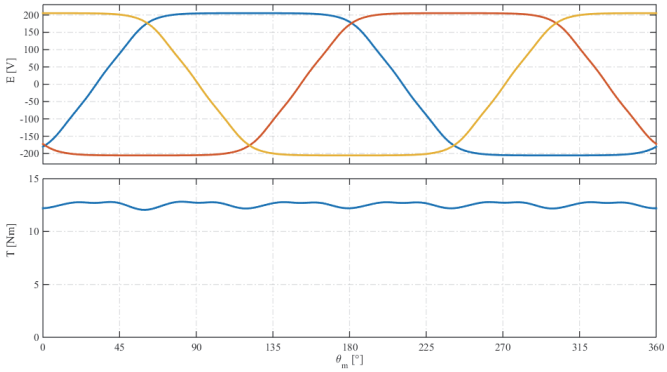


Fig. 10. Phase back-emfs (on the top) and torque (on the bottom) at $\omega_m$ = 30 krpm.

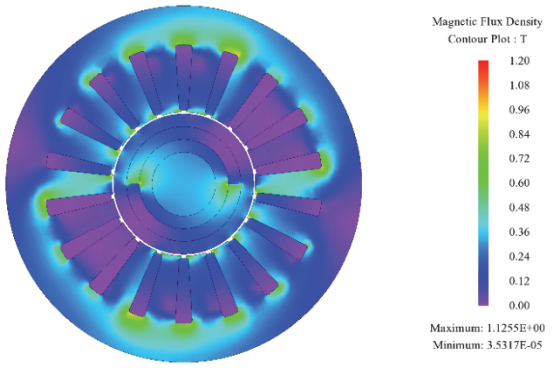


Fig. 11. Magnetic flux density at $\omega_m$ = 30 krpm and $T_e$ = 17.92 Nm.

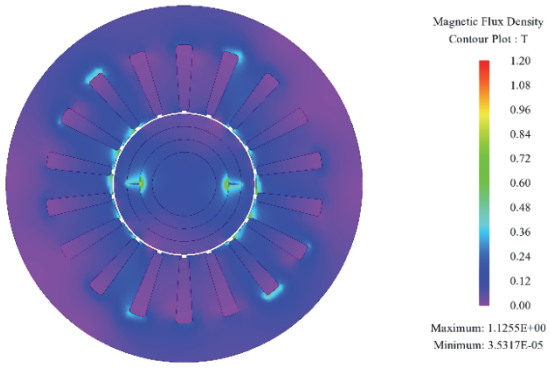


Fig. 12. Magnetic flux density at $\omega_m$ = 100 krpm and $T_e$ = 3.70 Nm.

TABLE IV
ANALYTICAL AND FEA RESULTS COMPARISON

| | Unit | Analytics | FEA |
|---|---|---|---|
| $P_n$ | kW | 40.0 | 39.45 |
| $T_e$ | Nm | 12.73 | 12.56 |
| $E$ | V | 204 | 205.4 |
| $\bar{B}_m$ | T | 0.254 | 0.249 |
| $\hat{B}_m$ | T | 0.178 | 0.164 |
| $\alpha$ | [-] | 0.70 | 0.66 |
| Iron Losses @ rated torque & speed | W | 338* | 302 |
| $\sigma_{eq}$ @100 krpm | GPa | 1.753 | 1.746 |
| $p_m$ @100 krpm | GPa | 0.061 | 0.057 |

*Computed in accordance with [23].

modified accordingly. However, it is worth noting that the proposed analytical approach has been developed for preliminary design purposes only. Consequently, these differences do not undermine the proposed approach, which enables a rapid and effective HS-BLDC preliminary design.

## V. CONCLUSION

The design of a novel High-Speed ferrite-based Brushless DC Machine (HS-BLDC) for electric vehicles has been presented. Mechanical and electromagnetic modeling have been addressed, which enable a rapid and effective HS-BLDC design that complies with both specific targets and operating constraints. The proposed approach has been validated by means of Finite Elements Analyses, which reveal a good matching with the analytical results. Further investigations will regard accurate copper losses and efficiency assessment together with thermal modeling at the aim of developing a prototype and experimental validation. These aspects will be investigated in future works.

## APPENDIX

In order to achieve pressures on PMs, reference can be made to the rotor cross section depicted in Fig. 2. Particularly, the radial displacement ($u_r$) on the contact surfaces of each rotor layer can be generally expressed as

$$u_r = \frac{r}{E}\left(\sigma_\theta - \upsilon\sigma_r\right) \tag{30}$$

in which $E$ and $\upsilon$ are the Young modulus and the Poisson ratio of the material respectively. By considering the contact surfaces between sleeve, PMs and rotor yoke, the following relationships are introduced

$$\begin{aligned}\left(u_r^{(s)} - u_r^{(m)}\right)\Big|_{r=r_m} &= D \\ \left(u_r^{(m)} - u_r^{(yr)}\right)\Big|_{r=r_{yr}} &= 0\end{aligned} \tag{31}$$

where $D$ is the radial interference. Hence, (30) can be properly substituted in (31), in which $\sigma_r$ and $\sigma_\theta$ expressions can be achieved by applying the Hooke's Law [15]. It is worth nothing that $\sigma_r$ and $\sigma_\theta$ depend on pressures on the contact surfaces of each rotor layer and, thus, appropriate boundary conditions have to be imposed as:

$$\begin{cases} p_i^{(yr)} = 0 \\ p_o^{(yr)} = -p_i^{(m)} \end{cases}, \quad \begin{cases} p_i^{(s)} = -p_o^{(m)} \\ p_o^{(s)} = 0 \end{cases} \tag{32}$$

where the subscripts $i$ and $o$ denote internal and external pressures respectively, whereas apexes $yr$, $m$ and $s$ refer to rotor yoke, PMs and sleeve. Therefore, the following equations are achieved

$$\begin{aligned} K_1 p_o^{(m)} + K_2 p_i^{(m)} &= D - C_{\omega 1} \\ K_3 p_o^{(m)} + K_4 p_i^{(m)} &= -C_{\omega 2} \end{aligned} \tag{33}$$

in which $K$ and $C$ depends on rotor geometry and materials as detailed by the following expressions:

$$K_1 = \frac{r_m}{E_s}\left(\frac{r_s^{\,2} + r_m^{\,2}}{r_s^{\,2} - r_m^{\,2}} + \upsilon_s\right) + \frac{r_m}{E_m}\left(\frac{r_m^{\,2} + r_{yr}^{\,2}}{r_m^{\,2} - r_{yr}^{\,2}} - \upsilon_m\right) \tag{34}$$

$$K_2 = -\frac{r_m}{E_m}\left(\frac{2r_{yr}^{\,2}}{r_m^{\,2} - r_{yr}^{\,2}}\right) \tag{35}$$

$$K_3 = -\frac{r_{yr}}{E_m}\left(\frac{2r_m^{\,2}}{r_m^{\,2} - r_{yr}^{\,2}}\right) \tag{36}$$

$$K_4 = \frac{r_{yr}}{E_m}\left(\frac{r_m{}^2 + r_{yr}{}^2}{r_m{}^2 - r_{yr}{}^2} + \upsilon_m\right) + \frac{r_{yr}}{E_{yr}}\left(1 - \upsilon_{yr}\right) \tag{37}$$

$$C_{\omega 1} = \frac{\omega_m{}^2}{4}\begin{pmatrix} \frac{r_m}{E_s}\left(\left(3+\upsilon_s\right)r_s{}^2 + \left(1-\upsilon_s\right)r_m{}^2\right)\rho_s + \\ -\frac{r_m}{E_m}\left(\left(3+\upsilon_m\right)r_{yr}{}^2 + \left(1-\upsilon_m\right)r_m{}^2\right)\rho_m \end{pmatrix} \tag{38}$$

$$C_{\omega 2} = \frac{\omega_m{}^2}{4}\begin{pmatrix} \frac{r_{yr}}{E_m}\left(\left(3+\upsilon_m\right)r_{yr}{}^2 + \left(1-\upsilon_m\right)r_m{}^2\right)\rho_m + \\ -\frac{r_{yr}}{E_{yr}}\left(\left(1-\upsilon_{yr}\right)r_{yr}{}^2\right)\rho_{yr} \end{pmatrix} \tag{39}$$

## ACKNOWLEDGMENT

Giuseppe Fois gratefully acknowledge Sardinia Regional Government for the financial support of his PhD scholarships (P.O.R. Sardegna F.S.E. Operational Programme of the Autonomous Region of Sardinia, European Social Fund 2007-2013 - Axis IV Human Resources, Objective l.3, Line of Activity l.3.1.).

## REFERENCES

[1] R. R. Moghaddam, "High speed operation of electrical machines, a review on technology, benefits and challenges," in *Proc. of IEEE Energy Conversion Congress and Exposition (ECCE 2014)*, Pittsburgh (USA), 2014, pp. 5539–5546.

[2] W. Gengji, Q. Qinglei, W. Ping, and W. Xiaoyuan, "Analysis of the rotor loss in a high speed permanent magnet motor for flywheel energy storage system," in *Proc. of 18th International Conference on Electrical Machines and Systems (ICEMS 2015)*, Pattaya (Thailand), 2015, pp. 2040–2044.

[3] Z. Kolondzovski, A. Arkkio, J. Larjola, and P. Sallinen, "Power Limits of High-Speed Permanent-Magnet Electrical Machines for Compressor Applications," *IEEE Trans. Energy Convers.*, vol. 26, no. 1, pp. 73–82, Mar. 2011.

[4] A. Tenconi, S. Vaschetto, and A. Vigliani, "Electrical Machines for High-Speed Applications: Design Considerations and Tradeoffs," *IEEE Trans. Ind. Electron.*, vol. 61, no. 6, pp. 3022–3029, Jun. 2014.

[5] D. Fodorean, "State of the Art of Magnetic Gears, their Design, and Characteristics with Respect to EV Application," in *Modeling and Simulation for Electric Vehicle Applications*, InTech, 2016.

[6] P. D. Pfister and Y. Perriard, "A 200 000 rpm, 2 kW slotless permanent magnet motor," in *Proc. of 11st International Conference on Electrical Machines and Systems (ICEMS 2008)*, Wuhan (China), 2008, pp. 3054–3059.

[7] J. F. Gieras, "Design of permanent magnet brushless motors for high speed applications," in *Proc. of 17th International Conference on Electrical Machines and Systems (ICEMS 2014)*, Hangzhou (China), 2014, pp. 1–16.

[8] D. Gerada, A. Mebarki, N. L. Brown, C. Gerada, A. Cavagnino, and A. Boglietti, "High-Speed Electrical Machines: Technologies, Trends, and Developments," *IEEE Trans. Ind. Electron.*, vol. 61, no. 6, pp. 2946–2959, Jun. 2014.

[9] I. Boldea, L. N. Tutelea, L. Parsa, and D. Dorrell, "Automotive Electric Propulsion Systems With Reduced or No Permanent Magnets: An Overview," *Ind. Electron. IEEE Trans. On*, vol. 61, no. 10, pp. 5696–5711, Oct. 2014.

[10] F. Martin, A. Belahcen, and M. E. H. Zaïm, "Effect of magnet materials on optimal design of a high speed PMSM," in *Proc. of 18th International Conference on Electrical Machines and Systems (ICEMS 2015)*, Pattaya (Thailand), 2015, pp. 661–667.

[11] K. H. Kim, H. I. Park, S. M. Jang, D. J. You, and J. Y. Choi, "Comparative Study of Electromagnetic Performance of High-Speed Synchronous Motors With Rare-Earth and Ferrite Permanent Magnets," *IEEE Trans. Magn.*, vol. 52, no. 7, pp. 1–4, Jul. 2016.

[12] A. Damiano, A. Floris, G. Fois, I. Marongiu, M. Porru, and A. Serpi, "Design of a High-Speed ferrite-based Brushless DC Machine for electric vehicles," in *Proc. of XXII International Conference on Electrical Machines (ICEM 2016)*, 2016, pp. 715–721.

[13] A. Serpi, G. Fois, F. Deiana, G. Gatto, and I. Marongiu, "Performance improvement of brushless DC machine by zero-sequence current injection," in *Proc. of 41st Annual Conference of the IEEE Industrial Electronics Society (IECON 2015)*, 2015, pp. 003804–003809.

[14] A. Rezzoug and M. E.-H. Zaim, Eds., *Non-conventional Electrical Machines*, 1 edition. Wiley-ISTE, 2013.

[15] R. G. Budynas, *Advanced Strength and Applied Stress Analysis*, 2 edizione. Boston: McGraw-Hill Higher Education, 1998.

[16] P. Moreno-Torres, M. Lafoz, M. Blanco, and J. R.Arribas, "Passenger Exposure to Magnetic Fields in Electric Vehicles," in *Modeling and Simulation for Electric Vehicle Applications*, InTech, 2016.

[17] U.S. Department of Energy (DOE), "Vehicle Technologies Office: 2015 Electric Drive Technologies Annual R&D Progress Report | Department of Energy."

[18] A. Serpi, "A flux-weakening predictive control algorithm for extended constant-power operation of surface-mounted PM machines," in *Proc. of 20th International Conference on Electrical Machines (ICEM 2014)*, Berlin (Germany), 2014, pp. 658–664.

[19] G. Gatto, I. Marongiu, A. Perfetto, and A. Serpi, "Three-Phase Operation of Brushless DC Motor Drive Controlled by a Predictive Algorithm," in *Proc. of 32nd Annual Conference on IEEE Industrial Electronics (IECON 2006)*, 2006, pp. 1166–1170.

[20] A. Damiano, F. Deiana, G. Fois, G. Gatto, I. Marongiu, A. Serpi, A. Perfetto, "Performance comparison between two-phase-on and three-phase-on operation of Brushless DC drives," in Proc. of 21st International Symposium on Power Electronics, Electrical Drives, Automation and Motion (SPEEDAM 2014), Ischia (Italy), 2014, pp. 489–494.

[21] R. Krishnan, *Permanent Magnet Synchronous and Brushless DC Motor Drives*. New York: CRC Press, 2010.

[22] D. Fodorean, "Study of a High-Speed Motorization With Improved Performances Dedicated for an Electric Vehicle," *IEEE Trans. Magn.*, vol. 50, no. 2, pp. 921–924, Feb. 2014.

[23] D. Eggers, S. Steentjes, and K. Hameyer, "Advanced Iron-Loss Estimation for Nonlinear Material Behavior," *IEEE Trans. Magn.*, vol. 48, no. 11, pp. 3021–3024, Nov. 2012.